**Showcasing the photothermal efficiency of narrow-NIR-responsive ultrasmall-in-nano architectures by the Research Unit coordinated by Dr Valerio Voliani at Center for Nanotechnology Innovation@NEST, Istituto Italiano di Tecnologia**

Photothermal effect by NIR-responsive excretable ultrasmall-in-nano architectures

Gold ultrasmall-in-nano architectures jointly combine efficient photothermal conversion and renal excretion of the building blocks. This approach might unlock the true potential of noble metal nanoplatforms for the treatment of neoplasms, filling the gap between bench-to-bedside.

As featured in:
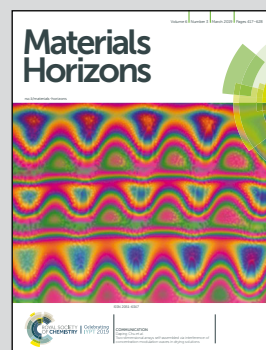
See Domenico Cassano, Valerio Voliani *et al.*, *Mater. Horiz.*, 2019, **6**, 531.

ROYAL SOCIETY OF CHEMISTRY | Celebrating IYPT 2019

rsc.li/materials-horizons

Photothermal effect by NIR-responsive excretable ultrasmall-in-nano architectures†

Domenico Cassano, [ID] ‡*[ab] Melissa Santi, [ID] ‡[a] Francesca D'Autilia,‡[ac]
Ana Katrina Mapanao,[ab] Stefano Luin [ID] [b] and Valerio Voliani [ID] *[a]

Photothermal therapy (PTT) is a promising (co)treatment with translation potentiality in oncology. Nowadays, the plasmonic nanoparticle-mediated photothermal effect (PT) relies on two well established NIR-responsive platforms: gold nanorods and nanoshells. Nonetheless, these nanostructures are affected by: (i) re-shaping after irradiation that prevents multiple PT treatments, and (ii) severe limitations to clinical translation due to metal persistence issues. Furthermore, evaluation of nanoparticle performance is usually accomplished *in vitro* or in mouse models, reducing the translational potential of the findings. Here, we report both the straightforward production of narrow-NIR-absorbing gold ultrasmall-in-nano architectures (*t*NAs) and their suitability as platforms for PT upon CW-irradiation at 808 nm. PT efficiency is fully assessed against 2D cell cultures and customized 3D pancreatic adenocarcinoma models. Remarkably, the morphology of the *t*NAs is not affected by laser irradiation, allowing for repeated PT cycles and preserving their ability to avoid long-term body persistence in excretory system organs.

Conceptual insights

The photothermal (PT) effect (*i.e.* light-to-heat non-radiative conversion) by gold nanoparticles (NPs) is a promising powerful tool for co-treatment of cancer diseases. Despite its unquestionable success in preclinical research, no noble metal PT transducer has obtained approval for clinical use either because: (i) NIR-absorption occurs for gold NPs whose size is above the renal excretion threshold or (ii) anisotropic ultrasmall gold NPs undergo reshaping after PT transduction. Herein, we demonstrate that narrow-NIR-responsive thermo nano-architectures (*t*NAs) bear the optimal size for renal excretion and sustain repeated series of NIR light-to-heat transduction without losing their functionalities, avoiding metal sintering or reshaping. Having addressed two key hurdles that currently hinder the clinical translation of PT therapy, this work provides a straightforward resolution for unleashing the potential of noble metals in cancer theranostics.

Introduction

Photothermal therapy (PTT) is a promising technique for non-invasive cancer treatment relying on the induction of tissue hyperthermia (HT), *i.e.* a localized temperature rising over 40 °C, by the conversion of light to heat.[1] An elegant approach to achieve a potential clinically relevant photothermal effect (PT) is through laser irradiation of noble metal nanoparticles (NPs) with localized surface plasmon resonances (LSPRs) in the first biological window (650–950 nm).[2] Commonly, NPs that exhibit LSPRs at near-infrared (NIR) frequencies are gold anisotropic structures, which include nanostars and nanorods.[2–5] Noticeably, also gold nanoshells have emerged as an excellent photothermal transducer, as their NIR optical response can be easily tuned by adjusting the diameter-to-shell thickness ratio.[6] However, despite the excellent light-to-heat conversion performances demonstrated by these nanoplatforms, only nanoshells have reached clinical trial evaluation, whereas nanorods and nanostars are still confined to the preclinical stage.[7] The failure of clinical translation of NP-mediated PTT is mainly ascribed to body persistence concerns.[8] Indeed, the optical response of nanostars and nanoshells can be tuned in the NIR region at the expense of an increase in NP diameter up to 150 nm.[6] On the other hand, body excretion of exogenous materials above 10 nm occurs through the hepatobiliary route that in the case of non-biodegradable noble metals is slow and inefficient.[9,10] As also communicated by the Scientific Committee on Emerging and Newly Identified Health Risks (SCENIHR), exogenous materials for healthcare have to be completely cleared from the body in a reasonable amount of time, avoiding persistence in the organism that would increase the likelihood of toxicity.[10] A commonly adopted approach to avoid metal persistence is to reduce NPs size below the threshold for renal

[a] Center for Nanotechnology Innovation@NEST, Istituto Italiano di Tecnologia, Piazza San Silvestro, 12-56126, Pisa, Italy. E-mail: valerio.voliani@iit.it

[b] NEST-Scuola Normale Superiore, Piazza San Silvestro, 12-56126, Pisa, Italy. E-mail: domenico.cassano@sns.it

[c] Unit of Advanced Optical Microscopy, Humanitas Clinical and Research Center, Rozzano, Milan, Italy

clearance, *i.e.* ultrasmall nanoparticles (USNPs).[11] Furthermore, the maximum light-to-heat transduction is obtained by NPs smaller than 5 nm, as the photothermal conversion efficiency is size-dependent.[12] Unluckily, LSPRs of excretable gold USNPs are in the UV/visible region, severely limiting their potential application in PTT as they are far from the first biological windows. In this regard, gold nanorods can partially avoid this issue. Indeed, at least one of their dimensions can be tailored in the ultrasmall range, suitable for renal excretion, while maintaining the LSPRs in the NIR.[13] However, gold nanorods re-shape into spheres during laser irradiation, preventing the possibility of multiple PTT series and resulting in non-excretable structures.[14–16] Strategies to preserve the nanorod morphology, such as silica coating, have been successfully adopted, albeit increasing their size.[17]

Here, we present a straightforward approach to combine body excretion of metals with NIR-triggered PTT by employing ultrasmall-in-nano architectures composed of metal USNPs embedded in biodegradable silica nanocapsules.[18,19] Based on this approach, our group has recently demonstrated the massive production of gold passion fruit-like nano-architectures (NAs) and their employment as biodegradable nanoplatforms for dual photoacoustic/ultrasound imaging and drug delivery (some routine characterizations are reported in Fig. S1, ESI†).[20–23] Their biodegradation to clearable building blocks has been observed in a number of biological environments in less than 48 h, including full human serum, human blood and cell cultures (Fig. S2, ESI†). Moreover, NAs' remarkable biocompatibility has been recently demonstrated in vertebrate models together with the daily quantitative evaluation of metal excretion by renal and hepatobiliary routes following biodegradation.[24,25] In particular, our group has recently demonstrated that biodegradable NAs can avoid the persistence of gold in organisms due to the interesting excretion rate of the building blocks from both renal and biliary pathways.[25]

So far, we have also demonstrated the versatility of the production protocol by the composition of NAs comprising USNPs of several noble metals and metal oxides.[26,27] Herein, we report the production of biodegradable and excretable narrow-NIR-responsive ultrasmall-in-nano architectures (thermo-NAs, *t*NAs) and demonstrate their behaviors as optimal platforms for PTT. Notably, while *t*NAs bear a substantially different optical behavior with respect to standard NAs, their production requires only a subtle modification to the original protocol. This is one of the most important points of strength of our approach, as the robustness of the synthetic protocols is a key-criterion for translatable nanotheranostics. Finally, the PT efficiency and HT efficacy of *t*NAs is fully-assessed on 2D cell cultures and significant 3D customized models of human pancreatic ductal adenocarcinoma (PDAC), remarkably enhancing their potentiality of translation from the pre-clinical to clinical investigation stage.

Results and discussion

Narrow-NIR-responsive *t*NAs displaying an overall diameter of 124.3 ± 23.0 nm were synthesized by employing slight modifications to the standard protocol for the production of NAs.[20]

Anionic gold USNPs were synthesized by fast reduction of an aqueous solution of chloroauric acid by sodium borohydride in the presence of poly(sodium 4-styrene sulfonate) (PSS). USNPs were partially aggregated by adding a DMF solution of (4,4′-dimercaptostilbene) (DMSB) and, finally, a controlled aggregation was obtained by adding an aqueous solution of cationic poly(L-lysine) (PLL). A 20 nm thick silica shell was then built on the USNP-polymer template by a modified Stöber process.[20] A typical wide-area TEM image of the *t*NAs is provided in Fig. S3 (ESI†), together with their size histograms. Noticeably, the entire protocol requires less than 4 h for the production of 15 mg of *t*NAs from a single operator, and the nanoplatforms have a value of about 1 € per mg by considering the raw materials. ICP-MS quantification on both NAs and *t*NAs revealed a slight difference in the amount of gold USNPs loaded in the nano-architectures, likely ascribed to the presence of DMSB in the *t*NAs. In particular, the gold loading, expressed as %w/w, is 4.9% and 3.8% for, respectively, NAs and *t*NAs. On the other hand, TEM images of *t*NAs reveal that they have the same overall morphology of standard NAs (Fig. 1A), whereas their optical behaviors differ substantially. The addition of DMSB induces a redshift of the main LSPR in the visible window from 530 to 570 nm in *t*NAs, and causes the appearance of another plasmonic band in the NIR region (Fig. 1B, background-subtracted extinction spectra).

We then performed DLS measurements on gold USNPs before the encapsulation in NAs and *t*NAs, in order to confirm their suitability for renal excretion. We found that both in the presence and absence of dithiol moieties, gold USNPs display a hydrodynamic diameter (HD) lower than 6 nm, (Fig. 1C). It is worth to notice that, upon biodegradation of the nano-architectures and the release of gold USNPs, the latter are likely coated by endogenous glutathione (GSH). Hence, we performed DLS measurements in a solution of GSH at a typical intra-cellular concentration (5 mM). We observed a slight decrease of the HD (Fig. 1C) in a few minutes, which remains in the ultrasmall range for both samples, confirming the suitability for renal excretion of USNPs.

Photothermal transduction efficiency was assessed by measuring the temperature increment of milliQ water-dispersed *t*NAs (1 mg mL^{-1}), stored in quartz cuvettes and irradiated with a pulsed laser at 808 nm under continuous stirring at laser output power varying between 0.4 W and 2.6 W. Temperature increment over 5 min was recorded with a 10 s time-step by means of a thermocouple in direct contact with the dispersion and with a thermal camera. Temperature increase up to 58 °C was recorded with the maximum laser power, whereas 1.1 W laser output resulted in the minimum power allowing the HT temperature threshold to be exceeded in about 250 s (Fig. S4, ESI†). Furthermore, the thermal images confirm that water-dispersed *t*NAs are uniformly heated up to 42 °C after 5 minutes of irradiation (Fig. 2A). It is worth noticing (Fig. 2B) that: (i) laser irradiation of both pure water or water solutions of nano-architectures devoid of metals (metal-free NAs, *mf* NAs) under the same experimental conditions results in a negligible temperature increase, and (ii) irradiation of standard NAs produced
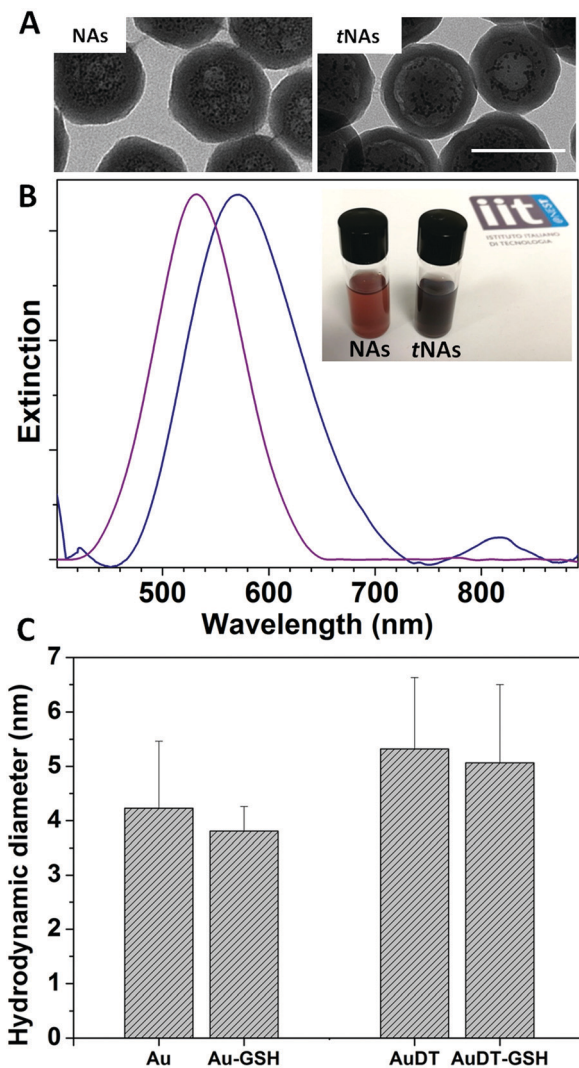
Fig. 1 (A) TEM images of NAs (left) and *t*NAs (right). Scale bar: 100 nm. (B) Background subtracted UV/vis absorbance spectra of NAs (purple) and *t*NAs (navy). Inset: 1 mg mL^{-1} water dispersions of the two samples. (C) Hydrodynamic diameters of gold USNPs (Au), GSH-coated gold USNPs (Au-GSH), dithiol-capped gold USNPs (AuDT) and GSH-coated AuDT (AuDT-GSH).

Fig. 2 (A) Thermal images of water and a 1 mg mL^{-1} *t*NAs water dispersion before and after 5 minutes of laser irradiation (808 nm, power 1.1 W). (B) Temperature trend of water (blue), *mf* NAs (green), NAs (red) and *t*NAs (black) upon irradiation at fixed laser output power (1.1 W) for 10 minutes. (C) PT cycles on the 1 mg mL^{-1} *t*NAs water dispersion. Irradiation: 10 minutes each. Red dotted line represents the temperature threshold for HT (40 °C).

a less efficient PT conversion with respect to *t*NAs, likely due to optical excitation on the tail of LSPR. Taken together, these findings confirm that PT conversion is due to a plasmonic effect rather than to the presence of silica and polymers. An interesting feature of *t*NAs is related to their potential employment for repeated photothermal cycles avoiding damage or re-shaping. Indeed, we assessed PT transduction efficacy at fixed laser output power 1.1 W, demonstrating that light-to-heat conversion is not affected after four cycles of 5 min each (Fig. 2C). Notably, TEM investigations revealed that, although intense laser irradiation induced the rupture of some nanocapsules, the overall morphology of *t*NAs is preserved (Fig. S5, ESI†). In particular, after four PT cycles no reshaping or sintering effect is produced on gold USNPs, which retain their optical behavior suitable for PT as well as their ideal ultrasmall size for renal clearance.[25]
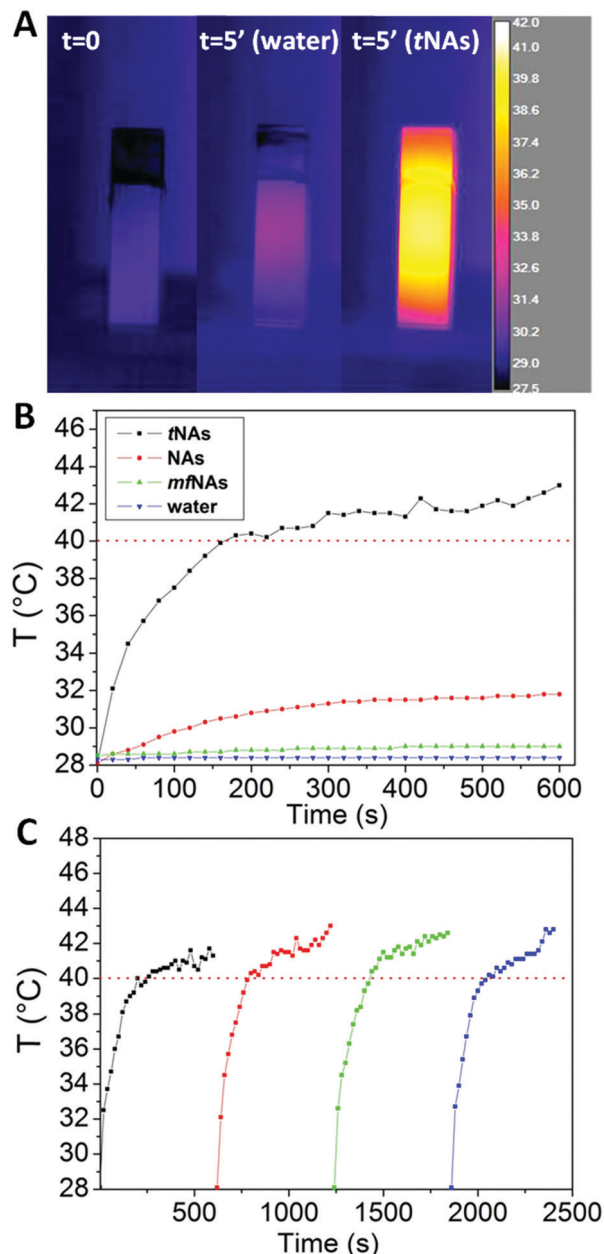
PT effect of *t*NAs was also evaluated on 2D and 3D models of PDAC. The choice of the MiaPaCa-2 cell line was determined by its particular aggressiveness and tendency to form metastases among PDAC models, and owing to our long-standing experience with this line, whose behavior has been fully assessed in our previous works.[23,28,29] In order to follow the cellular uptake of NAs and *t*NAs, AlexaFluor 647 dye was included into the nanocapsules, and imaging was performed through confocal fluorescence microscopy.[23] Fig. S6 (ESI†) shows the uptake of

both NAs and *t*NAs in 2D cultured MIA PaCa-2 cells after 2 h incubation. As expected, there is no appreciable difference between the cellular internalization of the two nanoarchitectures since their overall external morphology is preserved, confirming the robustness of the synthetic protocol. Notably, viability assays performed after 72 hours from the incubation, showed that the presence of DMSB in the *t*NAs does not induce a cytotoxic effect (Fig. S7, ESI†).

For studying PT treatment on 2D cultures, cells were incubated with NAs and *t*NAs (30 μg) for 2 hours and, then, laser irradiation was performed through confocal microscopy; a region of interest of 512 × 512 pixels (57 × 57 μm) was scanned with a pixel dwell time of 40 μs per pixel for 225 s employing a laser output power of 17 mW. This value was chosen as the maximum power not-inducing cellular death in the control samples (untreated cells) under the same irradiation timeframe. HT efficacy has been qualitatively evaluated through calcein-AM/propidium iodide (PI) cell staining. After the treatment, no sign of cellular death was found in the control (Fig. 3, top), yet there was a slight dimming of the green fluorescence likely due to calcein bleaching. On the other hand, HT induced by laser excitation of *t*NAs-treated cells caused substantial cellular death (Fig. 3, bottom). PT generated by NAs produced a less prominent cytotoxic effect (Fig. 3, center) in agreement with the PT efficiency assessments in water, as NAs

cause faint heating not sufficient to result in HT or to induce damage to cells.

Then, the cytotoxic effect of *t*NAs-induced HT was assessed on 3D models of PDAC. Findings obtained on 3D models have a more significant potentiality of translation with respect to both standard 2D cell cultures and subcutaneous xenograft *in vivo* models.[30] Furthermore, the development of customized 3D neoplasm models is in agreement with the 3R's concept, avoiding the sacrifice of animal models unless strictly necessary. Finally, 3D models enable potential investigations over the physiology of neoplasms in physiological conditions, including cell–cell and cell–extracellular matrix (ECM) interactions.[31,32] For example, light scattering from 3D multicellular spheroids has been previously investigated, reporting no significant dependence on the presence of cell-to-cell junctions or ECM, while scattered light's angular distribution is strictly dependent on the refractive indexes of different cellular compartments, exactly as in 2D models.[33] The 3D MIA PaCa-2 cell cultures were prepared through the hanging method, as fully described elsewhere.[29] Briefly, after 24 hours of drop suspension, the cell aggregates were transferred and maintained in an incubator with an orbital shaker for up to 1 month. The diameter of the obtained spheroids can range from 250 μm to about 1 mm. Herein, in order to both improve the significance of the comparison with samples and to approach models with a
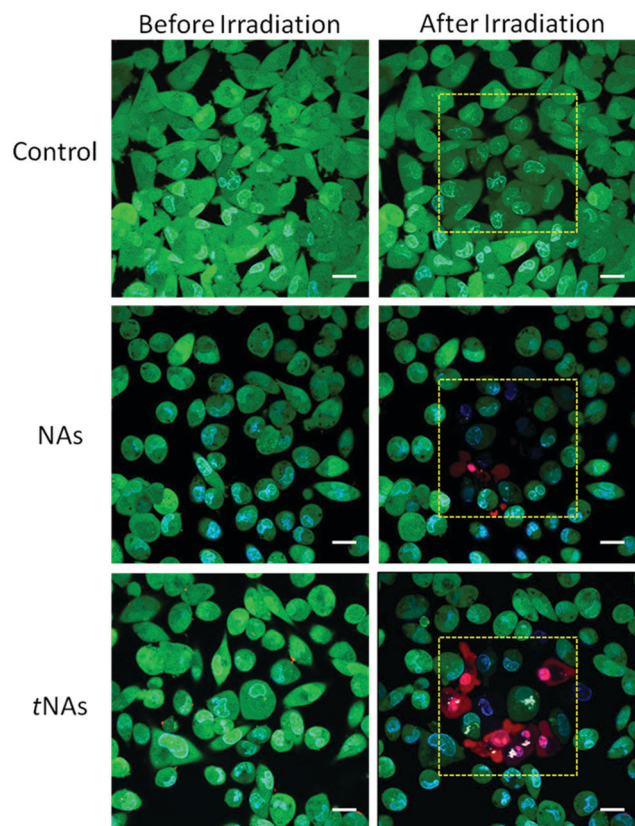
Fig. 3 Confocal images of NA and *t*NAs-treated Mia PaCa-2 cells before and after 808 nm pulsed laser irradiation. Yellow dashed squares depict the irradiated ROIs (57 × 57 μm). Green, blue and red LUTs represent calcein, Hoechst and PI, respectively. Scale bars: 10 μm.
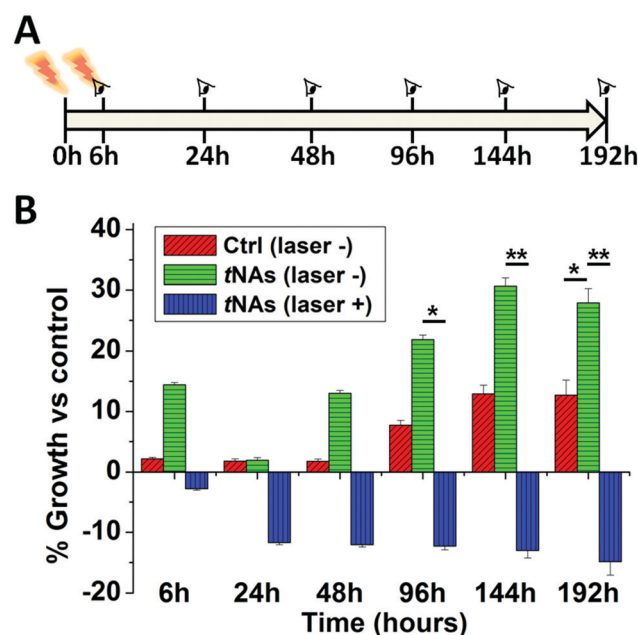
Fig. 4 (A) Spheroids were irradiated two times with a CW laser at 808 nm for 10 minutes (for a total of 20 minutes). The area of the models was measured for each time point for a total of 8 days. (B) Spheroid growth after irradiation. Red, green, and blue columns represent, respectively, not irradiated spheroids without or with *t*NAs and irradiated spheroids treated with *t*NAs. Results are expressed as the relative growth percentage of each sample with respect to the irradiated control without nanoparticles (corresponding to the 0% in the graph). Data are reported as the mean ± standard error of three independent experiments. Two-way ANOVA with Dunnett's test, *$p < 0.05$ and **$p < 0.01$.

micrometastasis resemblance (whose diameter is usually in the range of 0.2–2 mm), we have selected spheroids with a starting diameter of 350–450 μm (Fig. S8, ESI†).[34]

The best equilibrium between particle incubation and 3D model internalization was comprehensively investigated elsewhere for both bare and targeted NAs.[29] As expected, the internalization behavior of *t*NAs (Fig. S9, ESI†) resulted in agreement with NAs. HT efficacy was evaluated as spheroid growth inhibition over 192 hours after PT treatments. Spheroids were irradiated at 808 nm with an irradiance of 80 mW cm^{-2} for 10 minutes after 2 hours incubation with *t*NAs. The treatment was repeated after 6 hours with the same exposure conditions, and spheroid growth was monitored over 8 days (Fig. 4A).

Double irradiation was performed in order to damage cells both on the membranes and in the cytosol. Remarkably, spheroids were irradiated over their entire volume as, in our set-up, a semiconductor CW laser diode was employed in order to enhance the perspective of clinical translation. The irradiations produced a significant inhibition of the growth of the models treated by *t*NAs (Fig. 4B). On the other hand, *t*NAs themselves did not show any evidence of induced cytotoxicity. Indeed, models incubated with *t*NAs, yet not irradiated, demonstrated a regular growth similar to the not-irradiated control. Even if the PT treatment is not sufficient to induce complete spheroid death, the damage induced by laser irradiation has a major effect on cell viability (Fig. S10, ESI†) after 24 hours and results in growth inhibition that extends over days.

Conclusions

Overall, *t*NAs are the first reported NIR-absorbing plasmonic ultrasmall-in-nano platforms that jointly combine: (i) PT conversion efficacy suitable for HT, (ii) the possibility of multiple PT series and (iii) renal excretion of the building blocks after the therapeutic action. It is worth mentioning that *t*NAs sustain all the features of standard NAs, including the possibility of encapsulating drugs in their hollow cavity for HT-assisted chemotherapy. Their therapeutic effect has been assessed in valuable 3D models of human pancreatic adenocarcinoma. Moreover, tissue heating arising from NIR laser exposure could be effectively exploited for photoacoustic-guided HT, in order to employ a single nanostructure for simultaneous detection and treatment of diseases.

Materials and methods

AlexaFluor-647 was purchased from Invitrogen. All the other chemicals were provided by Sigma-Aldrich. Every reactant was used as it was without further purification.

Synthesis of passion fruit-like nano-architectures (NAs)

The following protocol is standardized for the production of 1.5 mg NAs in about 4 h. The protocol can be scaled-up to 20 mg.

Synthesis of gold nanoparticles. Ultrasmall gold nanoparticles with a diameter of approximately 3 nm were prepared according to the following procedure. To 20 mL of milliQ water, 10 μL of poly(sodium 4-styrene sulfonate) (70 kDa, 30% aqueous solution, PSS) and 200 μL of HAuCl$_4$ aqueous solution (10 mg mL^{-1}) were added. During vigorous stirring, 200 μL of sodium borohydride (8 mg mL^{-1} in milliQ water) was added quickly, and the mixture was vigorously stirred for 2 minutes. After the addition of NaBH$_4$, the solution underwent some color changes until becoming brilliant orange. Before its use, the solution was aged for 10 minutes and employed without further purification.

Synthesis of gold nanoparticle arrays. 20 mL of gold nanoparticle solution was added to a 50 mL round bottomed flask followed by 200 μL water solution of poly(ʟ-lysine) hydrobromide 15–30 kDa (PL, 20 mg mL^{-1}), and the mixture was allowed to stir for 20 minutes at room temperature. The as-synthesized gold aggregates were collected by centrifugation (13 400 rpm for 3 minutes), suspended in 2 mL of milliQ water and sonicated for a maximum of 4 minutes.

Synthesis of nano-architectures (NAs). 70 mL of absolute ethanol followed by 2.4 mL of ammonium hydroxide solution (30% in water), and 40 μL of tetraethyl orthosilicate (TEOS, 98%) were added in two 50 mL plastic Falcon tubes. The solution was allowed to stir for 5 minutes at RT. 2 mL of the gold nanoparticle arrays previously prepared were added to the Falcon (1 mL each) and the solution was allowed to gently shake for a further 3 h. The as-synthesized NAs were collected by 30 minutes centrifugation at 4000 rpm, washed twice with ethanol to remove unreacted precursors and suspended in 1 mL of ethanol. A short spin centrifugation was employed in order to separate the structures over 150 nm from the supernatant, which was recovered as a pink-iridescent solution. The solution containing about 1.5 mg of NAs was stored at −20 °C until use. It remains usually stable for at least 1 year. Product recovery: (i) 2 minutes centrifugation at 13 400 rpm, (ii) remove the colorless supernatant, and (iii) add the solvent of interest. The solubility of NAs in water, buffers, and physiological fluids is tested for up to 60 mg mL^{-1}.

Synthesis of thermoNAs (*t*NAs). *t*NAs were synthesized by following the same protocol employed for NAs, except that gold USNPs were partially aggregated by adding 200 μL of a DMF solution of (4,4′-dimercaptostilbene) (DMSB) 1 mg mL^{-1} prior to the formation of the arrays of PLL and PSS.

Electron microscopy. TEM observations of nanoparticles were carried out on a ZEISS Libra 120 TEM operating at an accelerating voltage of 120 kV, equipped with an in-column omega filter. The colloidal solutions were deposited on 300-mesh carbon-coated copper grids and observed after at least 5 h.

EDX point analysis. Energy dispersive X-ray spectroscopy (EDX) analysis was performed on the same microscope, working in scanning mode (STEM), thanks to a Bruker XFlash® 6 T|60 SDD detector.

ICP-MS measurements. NAs and *t*NAs were dissolved in 1 mL aqua regia (prepared with ICP-MS grade HCl and HNO$_3$) and digested under microwave irradiation (200 °C/15 minutes) in Teflon-lined vessels. The resulting solution was diluted to 10 mL with ICP-MS grade water, and Au content was determined by ICP-MS analysis against a standard calibration curve.

Cell culture. Human adenocarcinoma pancreatic cells (MIA PaCa-2) were purchased from the American Type Culture Collection (ATCC) and were maintained in Dulbecco's modified Eagle medium (DMEM) from Invitrogen (Carlsbad, CA). Growth medium was supplemented with 10% fetal bovine serum (FBS), 4 mM L-glutamine, 1 mM sodium pyruvate, 100 U mL^{-1} penicillin, and 100 mg mL^{-1} streptomycin (Invitrogen). Cells were maintained at 37 °C in a humidified 5% CO_2 atmosphere. For 3D structures, we used a modified protocol from Foty et al.[35] Briefly, cells were harvested and centrifuged for 5 min at 1200 rpm and then resuspended in fresh medium, counted and the suspension was adjusted to a final concentration of 1×10^6 cells per mL. Afterwarrds, 10 μL of cells were placed on the lid of a 60 mm cell culture dish that was flipped into the chamber containing 4 mL of PBS. Cells were allowed to settle into the drops until they form a sheet and then were transferred to a 35 mm suspension culture dish after 24 h. Finally, cell aggregates were placed inside a CO_2 incubator with an orbital shaker (90 rpm).

2D and 3D cell culture incubation with nanoparticles. For the experiment with 2D cell culture, cells were seeded 24 h before the experiment into a glass-bottom Petri dish (WillCo-dish GWSt-3522) to reach 80–90% of confluence. Cells were treated with NAs or tNAs (30 μg of each type of nanoparticles) for 2 h, washed twice with PBS and then maintained in fresh medium. For experiments with 3D structures, 100 μg of nanoparticles were used. Spheroids were treated for 2 h, washed twice with PBS and then transferred to 96-well round bottom plates with fresh medium.

Confocal microscopy on 3D models. In a 2 mL plastic vial, four to six cell constructs were collected using 1 mL pipet tips. The cells were settled and washed in PBS, whereas in 100 μL of PBS, Hoechst 33342 (Invitrogen; 80 μg mL^{-1}) and CellMask green plasma membrane stain (Invitrogen; 10 μg mL^{-1}) were added, and the cells were incubated at 37 °C and 5% CO_2 for 15 min. Afterward, the cells were washed twice with PBS, transferred to a LabTek 8-well chambered cover glass, and added with a 1:1 solution of 70% glycerol and FBS. Imaging was performed on an Olympus FV1000 inverted confocal laser scanning microscope equipped with a thermostat chamber set at 37 °C and 5% CO_2. The lasers for excitation were 405, 488, and 633 nm. Imaging was done 24 h after incubation. All images were analyzed using Fiji-ImageJ software version 1.51 s.

DLS measurements. The hydrodynamic diameter measurements were performed using a Malvern Zetasizer nano ZS90. During measurements, Au and AuDT colloids were suspended in milliQ water or in glutathione solutions (5 mM, milliQ water) for 15 minutes under vigorous stirring before the measure. The reported values are the average of ten measurements.

UV-vis spectrophotometry. The absorption spectra were obtained using a double-beam Jasco V-550 spectrophotometer. The samples were suspended in milliQ water and placed in quartz cuvettes with a 10 mm path length.

Photothermal experiments. To measure the photothermal activity of the nanoparticles, the samples (NAs or tNAs) were placed in a cuvette, stirred, and irradiated with a pulsed laser (typically employed for two-photon excitation) operating at 808 nm (Chameleon Vision, Coherent, Santa Clara, CA, USA). Each sample was irradiated for 10 min using 0.4, 1.1, 1.9 and 2.6 W and the increase of temperature was measured using a thermocouple inside the cuvette. For 2D imaging, cell viability was monitored using calcein-AM and propidium iodide (PI) to identify live and dead cells respectively. Samples were treated for 15 min with calcein-AM (2 μM), PI (1 μM) and Hoechst 33342 for nuclear staining. Treatments were performed with an Olympus FluoView FV1000 confocal microscope, coupled with a femtosecond Ti:Sapphire laser (Chameleon Vision, Coherent, Santa Clara, CA, USA). The laser beam was focused through a 60× NA 1.20 water immersion objective. All experiments were carried out at 37 °C and 5% CO_2 using an incubation chamber enclosing the microscope stage and body. The cells were visualized using a 405 nm diode laser to excite Hoechst, 488 nm Argon laser for excitation of calcein-AM and PI, and 633 nm HeNe laser to excite Alexa 647. The fluorescence emissions were collected with three detection channels, 410–480 nm for Hoechst, 500–590 nm for calcein-AM, and 610–710 nm for PI and Alexa 647 with the PMT detectors in analog mode. At first, an image was collected using a low zoom and a second one zooming in on the center of the area, and then PT treatment was done at 808 nm using 17 mW of power collecting a sequential image series (beam size at the focal spot can be estimated to be above ∼410 nm considering the diffraction-limited focusing with a numerical aperture NA of 1.2). The region of interest of 512 × 512 pixels (57 × 57 μm) was scanned with a pixel dwell time of 40 μs per pixel for 225 s. After the treatment, an image was taken reducing the zoom. For 3D experiments each spheroid was irradiated with a portable semiconductor diode laser at 808 nm for 10 min and then placed again in the incubator. The treatment was repeated after 6 h from the first one using the same parameters. The growth of the spheroids was measured immediately before both irradiation steps and then over time for 8 days. The growth of the spheroids was monitored using a Leica CTR 4000 epifluorescence microscope with a 10× air objective. For each spheroid the area was measured. Then the growth was calculated with respect to the initial area and expressed as the relative growth versus the control using the equation developed by Ménard et al.[36] All images, statistical tests and growth measurements were analyzed using ImageJ software version 1.48.

Viability assays. Cytotoxicity of tNAs was evaluated on 2D cell cultures by using a tetrazolium salt, 2-(2-methoxy-4-nitrophenyl)-3-(4-nitrophenyl)-5-(2,4-disulfophenyl)-2H tetrazolium, and monosodium salt (WST-8) assay. MIA PaCA-2 cells were seeded in 96-well plates with a density of 1×10^4 cells per well. After 24 h, the cells were incubated with tNAs for 2 h at 37 °C. After incubation, the medium was removed and the cells were washed twice with PBS and kept in fresh DMEM. For each experimental time point, cells were incubated with WST-8 reagent (10 μL) and 2% serum-containing medium (90 μL) for 2 h. Absorbance (450 nm) was measured using a microplate reader (Glomax Discovery, Promega). The percentage of cell viability was determined by comparing drug-treated cells with the untreated ones (100% viability).

The viability of 3D spheroids after irradiation was evaluated using the CellTiter-Glo® 3D Cell Viability Assay (Promega, Milan, Italy). Treated or untreated spheroids for each time point were transferred separately from a round bottom 96-well plate to a white 96-well plate for luminescence measurements with 100 μL of medium. Then 100 μL of CellTiter-Glo® 3D reagent was added to each well, the plate was shaken for 5 minutes and the luminescence signal was recorded after 25 minutes of incubation with a microplate reader (Glomax Discovery, Promega).

Conflicts of interest

The authors declare no conflicts of interest.

Acknowledgements

References

1 X. Huang, P. K. Jain, I. H. El-Sayed and M. A. El-Sayed, *Photochem. Photobiol.*, 2006, **82**, 412.

2 M. F. Tsai, S. H. G. Chang, F. Y. Cheng, V. Shanmugam, Y. S. Cheng, C. H. Su and C. S. Yeh, *ACS Nano*, 2013, **7**, 5330–5342.

3 Y. Liu, X. Zhi, M. Yang, J. Zhang, L. Lin, X. Zhao, W. Hou, C. Zhang, Q. Zhang, F. Pan, G. Alfranca, Y. Yang, J. M. de la Fuente, J. Ni and D. Cui, *Theranostics*, 2017, **7**, 1650–1662.

4 I. G. Theodorou, Z. A. R. Jawad, Q. Jiang, E. O. Aboagye, A. E. Porter, M. P. Ryan and F. Xie, *Chem. Mater.*, 2017, **29**, 6916–6926.

5 A. Li Volsi, C. Scialabba, V. Vetri, G. Cavallaro, M. Licciardi and G. Giammona, *ACS Appl. Mater. Interfaces*, 2017, **9**, 14453–14469.

6 R. S. Riley and E. S. Day, *Wiley Interdiscip. Rev.: Nanomed. Nanobiotechnol.*, 2017, **9**, e1449.

7 A. C. Anselmo and S. Mitragotri, *AAPS J.*, 2015, **17**, 1041–1054.

8 F. Chen and W. Cai, *Nanomedicine*, 2015, **10**, 1–3.

9 T. Sun, Y. S. Zhang, B. Pang, D. C. Hyun, M. Yang and Y. Xia, *Angew. Chem., Int. Ed.*, 2014, **53**, 12320–12364.

10 Y. Vlamidis and V. Voliani, *Front. Bioeng. Biotechnol.*, 2018, **6**, 143.

11 E. Lim, T. Kim, S. Paik, S. Haam, Y. Huh and K. Lee, *Chem. Rev.*, 2015, **115**, 327–394.

12 K. Jiang, D. A. Smith and A. Pinchuk, *J. Phys. Chem. C*, 2013, **117**, 27073–27080.

13 F. Zhao, X. Li, J. Li, Y. Dou, L. Wang, M. Wu, Y. Liu, J. Chang and X. Zhang, *J. Mater. Chem. B*, 2017, **5**, 2145–2151.

14 M. Gordel, J. Olesiak-Banska, K. Matczyszyn, C. Nogues, M. Buckle and M. Samoc, *Phys. Chem. Chem. Phys.*, 2014, **16**, 71–78.

15 G. González-Rubio, A. Guerrero-Martínez and L. M. Liz-Marzán, *Acc. Chem. Res.*, 2016, **49**, 678–686.

16 N. Katchinskiy, R. Godbout, A. Hatef and A. Y. Elezzabi, *Adv. Ther.*, 2018, **1**, 1800009.

17 Y.-S. Chen, W. Frey, S. Kim, K. Homan, P. Kruizinga, K. Sokolov and S. Emelianov, *Opt. Express*, 2010, **18**, 8867.

18 D. Cassano, S. Pocoví-Martínez and V. Voliani, *Bioconjugate Chem.*, 2018, **29**, 4–16.

19 J. G. Croissant, Y. Fatieiev and N. M. Khashab, *Adv. Mater.*, 2017, **29**(9), 1604634.

20 D. Cassano, D. Rota Martir, G. Signore, V. Piazza and V. Voliani, *Chem. Commun.*, 2015, **51**, 9939–9941.

21 C. Avigo, D. Cassano, C. Kusmic, V. Voliani and L. Menichetti, *J. Phys. Chem. C*, 2017, **121**, 6955–6961.

22 P. Armanetti, S. Pocoví-Martínez, A. Flori, C. Avigo, D. Cassano, L. Menichetti and V. Voliani, *Nanomedicine*, 2018, **14**, 1787–1795.

23 D. Cassano, M. Santi, V. Cappello, S. Luin, G. Signore and V. Voliani, *Part. Part. Syst. Charact.*, 2016, 818–824.

24 M. D'Amora, D. Cassano, S. Pocoví-Martínez, S. Giordani and V. Voliani, *Nanotoxicology*, 2018, 914–922.

25 D. Cassano, M. Summa, S. Pocoví-Martínez, A.-K. Mapanao, T. Catelani, R. Bertorelli and V. Voliani, *Part. Part. Syst. Charact.*, 2018, 1800464.

26 S. Pocoví-Martínez, D. Cassano and V. Voliani, *ACS Appl. Nano Mater.*, 2018, **1**, 1836–1840.

27 D. Cassano, J. David, S. Luin and V. Voliani, *Sci. Rep.*, 2017, **7**, 43795.

28 M. H. Katz, S. Takimoto, D. Spivack, A. R. Moossa, R. M. Hoffman and M. Bouvet, *Clin. Exp. Metastasis*, 2004, **21**, 7–12.

29 A. K. Mapanao, M. Santi, P. Faraci, V. Cappello, D. Cassano and V. Voliani, *ACS Omega*, 2018, **3**, 11796–11801.

30 S. J. Jackson and G. J. Thomas, *Dis. Models Mech.*, 2017, **10**, 939–942.

31 S. Nath and G. R. Devi, *Pharmacol. Ther.*, 2016, **163**, 94–108.

32 H. Lu and M. H. Stenzel, *Small*, 2018, **14**, 1702858.

33 J. R. Mourant, T. M. Johnson, V. Doddi and J. P. Freyer, *J. Biomed. Opt.*, 2002, **7**, 93.

34 P. Hermanek, R. V. P. Hutter, L. H. Sobin and C. Wittekind, *Cancer*, 1999, **86**, 2668–2673.

35 R. Foty, *J. Visualized Exp.*, 2011, DOI: 10.3791/2720.

36 M. Ménard, F. Meyer, K. Parkhomenko, C. Leuvrey, G. Francius, S. Bégin-Colin and D. Mertz, *Biochim. Biophys. Acta, Gen. Subj.*, 2019, **1863**, 332–341.